Journal Pre-proof

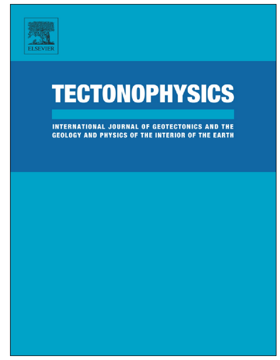

Dynamic triggering of earthquakes and the role of overpressure fluids in active geothermal areas in Yunnan, China

Zhiwei Wang, Xinglin Lei, Shengli Ma, Hong Fu, Xiaojing Hu, Kaiying Wang, Yusuke Mukuhira, Changrong He

PII: S0040-1951(24)00163-X

DOI: https://doi.org/10.1016/j.tecto.2024.230361

Reference: TECTO 230361

To appear in: *Tectonophysics*

Received date: 10 October 2023

Revised date: 16 April 2024

Accepted date: 21 May 2024

Please cite this article as: Z. Wang, X. Lei, S. Ma, et al., Dynamic triggering of earthquakes and the role of overpressure fluids in active geothermal areas in Yunnan, China, *Tectonophysics* (2023), https://doi.org/10.1016/j.tecto.2024.230361

Dynamic triggering of earthquakes and the role of overpressure fluids in active geothermal areas in Yunnan, China

Zhiwei Wang[1,3*], Xinglin Lei[2], Shengli Ma[1], Hong Fu[4], Xiaojing Hu[4], Kaiying Wang[1], Yusuke Mukuhira[3] and Changrong He[1]

[1] State Key Laboratory of Earthquake Dynamics, Institute of Geology, CEA, Beijing, China

[2] Geological Survey of Japan, AIST, Ibaraki, Japan

[3] Institute of Fluid Science, Tohoku University, Sendai, Japan

[4] Yunnan Earthquake Agency, Yunnan, China

Corresponding author: zhiwei-wang@ies.ac.cn

Highlights:

- Seismicity in the Yunnan area is sensitive to dynamic stress caused by distant strong earthquakes.
- The ETAS models reveal a high proportion of forced seismicity and a weak magnitude-dependent aftershock productivity.
- Triggered clusters repeatedly manifested in specific fault structures with enhanced fluid permeability.

Abstract

The Yunnan area is rich in geothermal fluids, and thus seismicity in this region is considered to be sensitive to stress turbulence by earth tides and distant strong earthquakes. We have identified 13 distant strong earthquakes out of 110 that have dynamically triggered seismicity with a statistical significance of β value greater than 2 and β_e. The triggered seismic clusters show the following features. 1) Most clusters are distributed at special fault locations such as fault ends, fault bends, fault steps, and fault intersections. 2) Some clusters display clear fluid diffusion processes, with an increasing water temperature in nearby wells. 3) The ETAS models show a high proportion of forced seismicity and a weak dependence on magnitude for aftershock productivity. These results suggest that the triggered seismicity in the Yunnan area tends to concentrate in specific fault structures with enhanced fluid permeability, where the presence of overpressured fluids possibly makes the seismicity sensitive to dynamic stress triggering.

1. Introduction

Dynamic triggering, caused by passing seismic waves [*Brodsky and van der Elst*, 2014], results in oscillating stress perturbance on the fault plane, accelerating the fault rupture process and potentially causing immediate failure if the fault is critically stressed [*Perfettini et al.*, 2003]. Unlike static triggering, which occurs due to stress changes from nearby fault slips, seismic waves from a distant earthquake do not produce a stress shadow zone. Additionally, dynamic stress decays more slowly with distance than static stress [*Kilb et al.*, 2000].

Understanding dynamically triggered seismicity provides insights into identifying fault segments that are at a critical stress level and quantifying the stress required to trigger fault failure. This is accomplished by statistically analyzing the spatial-temporal variation of seismicity before and after distant strong earthquakes [*Hill et al.*, 1993]. Furthermore, seismic waves have the potential to trigger abnormal changes in subsurface fluids [*Brodsky*, 2003]. Consequently, the role of deep overpressured fluids in dynamic triggering is a compelling yet not fully understood key issue in seismology [*Aiken et al.*, 2018; *Alfaro-Diaz et al.*, 2022; *Brodsky and Prejean*, 2005; *DeSalvio and Fan*, 2023; *Fan et al.*, 2021; *Guenaga et al.*, 2021; *Lei et al.*, 2011a; *Miyazawa et al.*, 2021; *Prejean and Hill*, 2018; *N. J. van der Elst et al.*, 2013; *B Wang et al.*, 2018; *Yao et al.*, 2021; *Yukutake et al.*, 2013].

Dynamic triggering is frequently observed in regions such as geothermal and volcanic areas, extensional zones, and areas of high strain rates [*Hill and Prejean*, 2015]. In certain instances, the arrival of surface waves or coda waves of distant strong earthquakes can immediately trigger seismic activity [*Hill et al.*, 1993; *Lei et al.*, 2011a; *Yukutake et al.*, 2013]. For instance, following the 2011 Tohoku M9 earthquake, there was a rapid increase in seismicity below the Hakone volcano in central Japan, located approximately 450 km away [*Yukutake et al.*, 2013]. In other areas, dynamic triggering shows delayed effects, ranging from hours to months [*Brodsky*, 2006; *Johnson and Bürgmann*, 2016; *Peña Castro et al.*, 2018]. For example, approximately 7 hours after the 2016 Mw7.8 Ecuador earthquake, a statistically significant increase in seismicity was observed in the wastewater injection field in north Oklahoma, USA [*Peña Castro et al.*, 2018].

Previous studies have proposed various mechanisms to explain dynamic triggering, including the frictional properties model [*Voisin*, 2002], the Coulomb failure model [*Voisin et al.*, 2004], and the subcritical crack growth model [*Brodsky and Prejean*, 2005]. However, these models fail to account for delayed triggering. Fluids and pore pressure mechanisms, on the other hand, offer an explanation for the delayed triggering through processes such as fluid diffusion, pore pressure changes, and liquid dissolution [*Brodsky*, 2003]. Nevertheless, many case studies lack definitive evidence of deep-seated fluids. The role of fluids is often inferred through a chain of circumstantial evidence. For example, the ETAS (epidemic type aftershock sequence) model effectively reveals the temporal and spatial variation in seismicity [*Ogata*, 1992; *Zhuang et al.*, 2002], aiding in the identification of signs of fluid-triggered seismicity related to both industrial injections [*Lei et al.*, 2013] and natural fluid [*Su et al.*, 2023].

The dynamic triggering in Yunnan, China, known for its abundance of hydrothermal fluids [*Shangguan et al.*, 2000], has been the subject of investigation in many previous studies [*Lei et al.*, 2011a; *L Li et al.*, 2019; *G Peng et al.*, 2021]. Notably, the 2004 Sumatra Mw9.3 earthquake triggered 10 seismic clusters across a wide area, occurring at fault ends, bends, step-overs, and intersections. These geological features serve as permeable channels with hot springs, suggesting a potential link between geothermal fluids and the triggered seismic activities [*Lei et al.*, 2011a].

In this study, we conducted a comprehensive investigation of dynamic triggering in the Yunnan geothermal region from 2006 through 2021, utilizing seismic data collected from permanent stations and 30 temporary stations installed in February 2018 and the template matching method. The rest of this article is organized as follows. **Section 2** describes the primary methods employed in the study, which includes earthquake detection and location, the ETAS model, and the β statistic. **Section 3** presents the results of dynamic triggering observed from 2006 through 2018.

Section 4 focused on dynamic triggering during the period from March 2018 to 2021, with particular attention to the period following the 2019 Laos Mw 6.2 earthquake. Finally, **Section 5** delves in to a discussion of key issues and provides concluding remarks.

2. Methods

2.1. Microseismic detection and hypocenter relocation

We collected continuous seismic waveform data from February 25, 2018, to 2021, utilizing recordings from 14 permanent broadband stations and 30 temporary short-period stations. Between April 15 and April 30, 2018, data recording ceased for 30 temporary seismic stations. The stations are strategically located within the region spanning from 99° to 101° in longitude and 25° to 27° in latitude (Fig. 1). To detect and locate seismic events, we employed the waveform correlation method using continuous seismic waveform data collected from February 25, 2018, to 2021, as described in [*Z Peng and Zhao*, 2009; *Zhang et al.*, 2022; *Zhang and Wen*, 2015]. In our analysis, we used the 3D USTClitho2.0 velocity model, which was derived by combining both body wave and surface wave data [*Han et al.*, 2021].

We began by selecting 4459 template events from the catalog published by the China Earthquake Network Center (CENC), applying criteria such as M (magnitude) $\geq$ 1.0, a station count of $\geq$3, and a Signal-to-noise ratio (SNR) $\geq$ 3.0. Initially, we performed a preliminary relocate these template events using the HypoDD method [*Waldhauser and Ellsworth*, 2000], using manually picked P and S arrival times for the permanent stations compiled by CENC. Subsequently, for the period when data from the temporary stations were available, we refined the template events relocations by incorporating P and S arrival times determined by the Akaike Information Criteria (AIC) method [see *Lei et al.*, 2022 and reference within for details] for temporary stations. During the relocation process, we maintained a maximum distance of 10 km between earthquakes in a pair and ensured a minimum 8 links. In the end, we successfully improved the hypocenter accuracy for 1311 templates, covering the period from February 25, 2018, to 2021.

We applied the Template Matching method, which relies on multi-channel waveform cross-correlation, to detect and locate potential events of small magnitude and events excluded during the relocation processes. At first, we applied a band-pass filter (1 and 10 Hz) and reduced the sampling rate to 50 Hz for both the template and continuous waveforms to expedite computations. For the P-wave, we defined a time window of 1 second before and 5 seconds after the P-wave arrival time, while for the S-wave, the time window extended from 1 second before to 10 seconds after the S-wave arrival time.

To determine the relative location of potential events, we employed a grid search approach, as outlined in [*Zhang and Wen*, 2015]. For each template, the grid is centered at the template's hypocenter, with a maximum horizontal and vertical search distance of 2 km and a grid spacing of 0.1 km and 0.2 km in horizontal and vertical directions, respectively. The travel time difference between the template event and each grid point was calculated and the used in the calculation of the correlation coefficient (CC) for each pair of waveforms. The stacked average CC and SNR were instrumental in identifying potential events and their respective locations. Specifically, we applied a CC threshold of 0.3 and a SNR threshold of 10 for event detection [*Tang et al.*, 2018; *Z Wang et al.*, 2020; *Zhang and Wen*, 2015]. Furthermore, we calculated the magnitude by comparing the peak S-wave amplitudes of the template earthquake to these of the potential earthquake. In total, our analysis reveals 31,806 events.

2.2. β-statistic

We use β-statistics to map the spatial variation in seismicity rate changes following a given event [*Aiken and Peng*, 2014 ; *Aron and Hardebeck*, 2009; *Lei et al.*, 2011a; *Matthews and Reasenberg*, 1988; *Reasenberg and Simpson*, 1992]. The β values ≥ 2 and ≤ -2 indicate a significant increase and decrease in the seismicity rate, as detailed by Hill and Prejean (2015). The β-statistic is given by:

$$\beta = \frac{N_a - N * T_a/T}{\sqrt{N(T_a/T)(1 - T_a/T)}} \quad 1)$$

where N_a represents the number of events within the specific time window T_a. *N* is the total number of events during the entire time window *T*, which includes both the background time window T_b and the specific time window T_a. It's important to ensure that the duration of *T* is sufficiently long to estimate a reliable mean rate of background seismicity and its standard error.

To map the β values, we partitioned the research area into a grid of 101×101 cells and compute the β value at each grid point. To ensure the reliability of the β value calculation for a specific grid, we required a minimum of 40 events within the total time span, all occurring within a maximum radial distance of 15 km from that grid point. Grids with an insufficient number of events to meet these criteria were assigned a β-value of zero.

After identifying triggered clusters with β values greater than 2, we adopted a methodology similar to the approach proposed by Li et al. (2023)[*C Li et al.*, 2023]. This method allowed us to differentiate seismicity increases due to dynamic triggering from those attributed to random fluctuations. It involved establishing an empirical β value threshold, denoted as β_e, associated with each distant shock. However, due to the longer time span of our dataset, 2006-2021, if we take the entire window after possible triggering events (i.e., distant earthquakes) as the upper limit of Ta, there are some cases of Ta much larger than Tb. It is possible to include some occasional swarms having large number of events, and the entire sequence is no longer stable. As an improvement, we require Ta to be not greater than Tb. Furthermore, we only used 5000 random Ta, and the results were no different from those of 10000.

2.3. Peak dynamic stress

We first computed Peak Ground Velocity (PGV) values from the observed surface waves, using a band-pass filter of 0.01~0.2Hz. Subsequently, we applied the formula σ_{pd}= PGV*G/c to calculate the peak dynamic stress value, where σ_{pd} is the peak dynamic stress value, G is the shear modulus (32GPa), c is the shear-wave velocity (3.5km/s) [*Peña Castro et al.*, 2018; *Nicholas J. van der Elst and Brodsky*, 2010; *Velasco et al.*, 2004].

2.4. Epidemic-Type Aftershock Sequence (ETAS) Model

We constructed an ETAS model to analyze the earthquake triggering relationship and characterize seismicity features, drawing from previous studies [*Lei et al.*, 2013; *Lei et al.*, 2019; *Ogata*, 1992; *Zhuang et al.*, 2002]. In ETAS modeling, the total occurrence rate $\lambda(t)$ of seismicity is divided into two components. The first part represents background (also termed as forced to emphasize that these seismic activities are driven by some external forces, such as tectonic loading, aseismic sliding, and fluid pressure) seismicity $\lambda_0(t)$, which we assume varies with time. The second part represents the earthquake contribution before the *i-th* event $\xi(t; t_i, m_i)$, and we assume it depends on the occurring time of the previous events . The relationship is as follows:

$$\lambda(t) = \lambda_0(t) + \sum_{i:t_i<t} \xi(t; t_i, m_i) \qquad 2)$$

$$\xi(t; t_i, m_i) = \kappa(m_i) g(t - t_i) \qquad 3)$$

$$\kappa(m) = Ae^{\alpha(m-m_c)}, m \geq m_c \qquad 4)$$

$$g(t) = \frac{p-1}{c}\left(1 + \frac{t}{c}\right)^{-p}, t > 0 \qquad 5)$$

t_i: represents the time when the *i-th* event occurred. m_c: denotes the magnitude of completeness for the catalog. α: signifies the aftershock production capacity. p: represents the aftershock attenuation rate. c and A: denotes the constants involved in the modified Omori's law. For specific details regarding the calculation process of these parameters, please refer to [*Lei et al.*, 2013] for the specific parameter calculation process.

3. Results for the period from 2006 to 2018

We gathered a dataset comprising 8,093,375 P arrivals and 8,239,700 S arrivals recorded across 63 permanent seismic stations for a total of 24,462 events occurring between 2006 to February 25, 2018. The catalogs magnitude of completeness (Mc) is 1.5 (Fig. 1). Employing the HypoDD method, we successfully relocated 7,968 events with improved hypocenter accuracy (Fig. 2).

Between 2006 and 2021, we analyzed 110 long-distant earthquakes with a magnitude (M) of 6.0 or greater, resulting in peak dynamic stresses exceeding 1.0 kPa in the research area, as illustrated in Figure 2. Subsequently, we mapped β distributions following these earthquakes, using a time window (T_a) of 14 days and a maximum radial distance of 15 km were used in the β statistics. The window length of 14 days is determined following [*Lei et al.*, 2011a], representing the typical duration of dynamically triggered seismicity clusters from the 2004 Sumatra earthquake. The threshold of β >2 and β >β_e was chosen as an indicator of statistically significant seismicity increase[*C Li et al.*, 2023]. It is considered that dynamic triggering has occurred if just one location reaches the β triggering threshold. Our analysis revealed that 13 earthquakes were followed by a significant increase in the seismicity rate, with multiple locations having β values greater than 2 and β_e, as depicted in Figure 3 and summarized in Table 2. These dynamically triggered seismic clusters were notably concentrated at fault ends, step-overs, bends, and fault intersections. Remarkably, more than ten spots experienced dynamically triggering on at least two occasions.

Of particular interest is the source region of the 2021 Ms 6.4 Yangbi earthquake sequence, one of the major events in our study area. It is noteworthy that this source region is surrounded by triggered clusters, yet no triggered seismicity was observed within the source region itself.

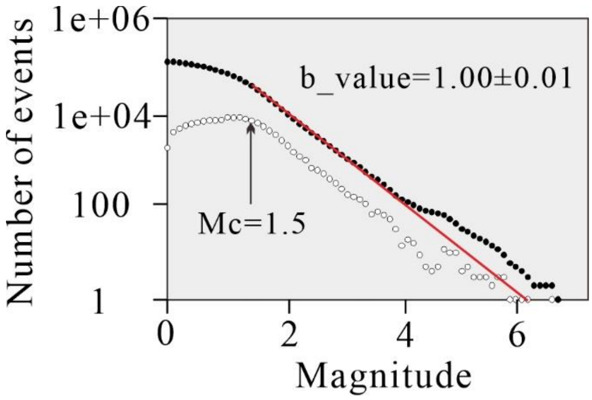

Figure 1. Frequency–magnitude distribution spanning the years 2006 to 2018. The seismic b-value, estimated using the Maximum Likelihood Method, is depicted by the red line. The white dots represent the seismic frequency, while the black dots represent the cumulative numbers. The catalog is sourced from the National Earthquake Data Center and can be accessed at http://data.earthquake.cn.

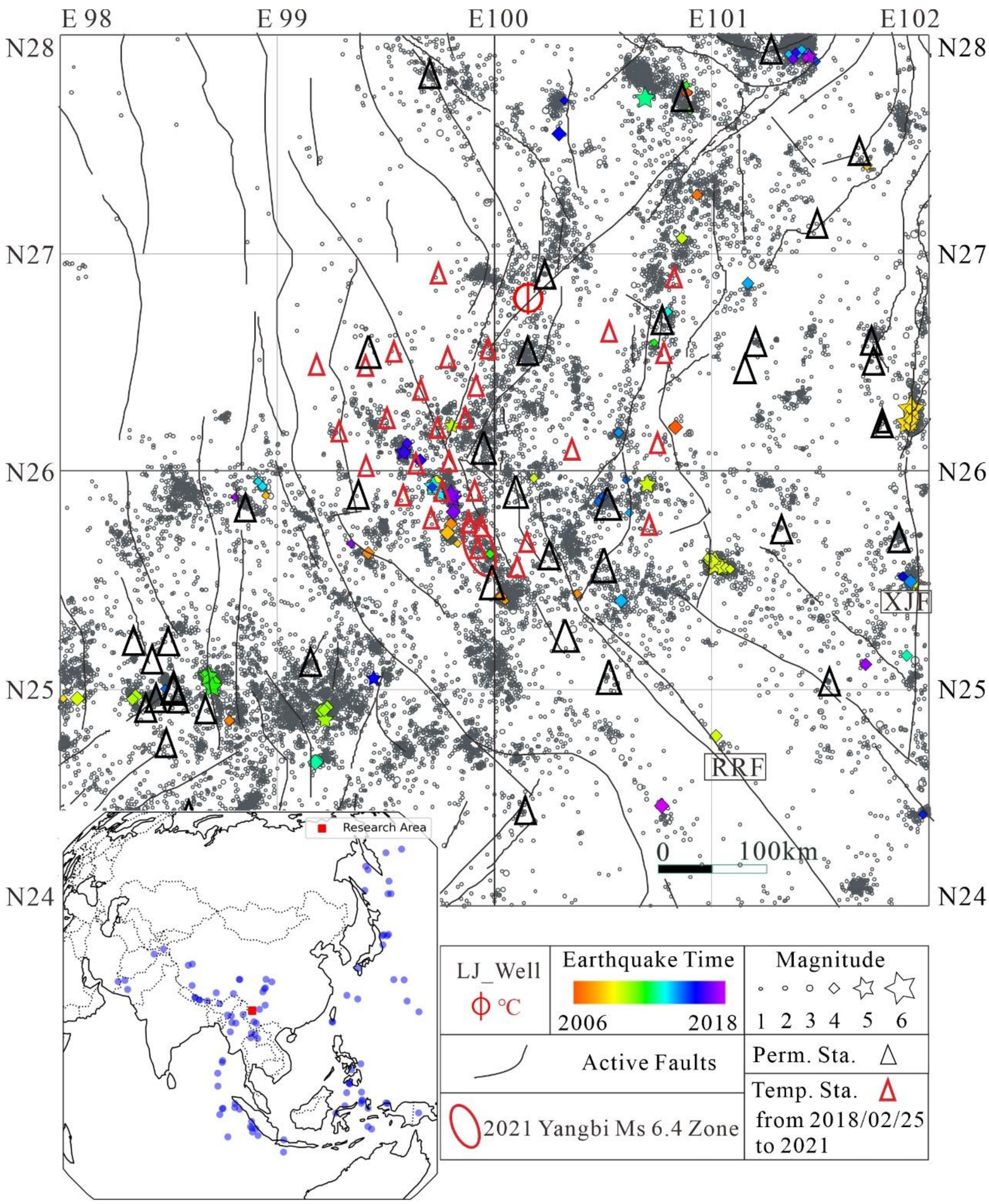

Figure 2. Map view of Yunnan study area, relocated earthquakes, faults, and distant strong earthquakes. Colored earthquakes indicate the occurrence time of events with a magnitude greater than 4. LJ_Well: LiJiang water temperature well. RRF: Red River Fault. XJF: XiaoJiang Fault. In the rectangle inset, the red box is the research area. The blue dots represent long-distance strong earthquakes with a magnitude (M) greater than 6, triggering dynamic stress peaks exceeding 1.0 kPa. The M>6 Catalog is sourced from the USGS and can be accessed at https://www.usgs.gov/programs/earthquake-hazards/earthquakes.

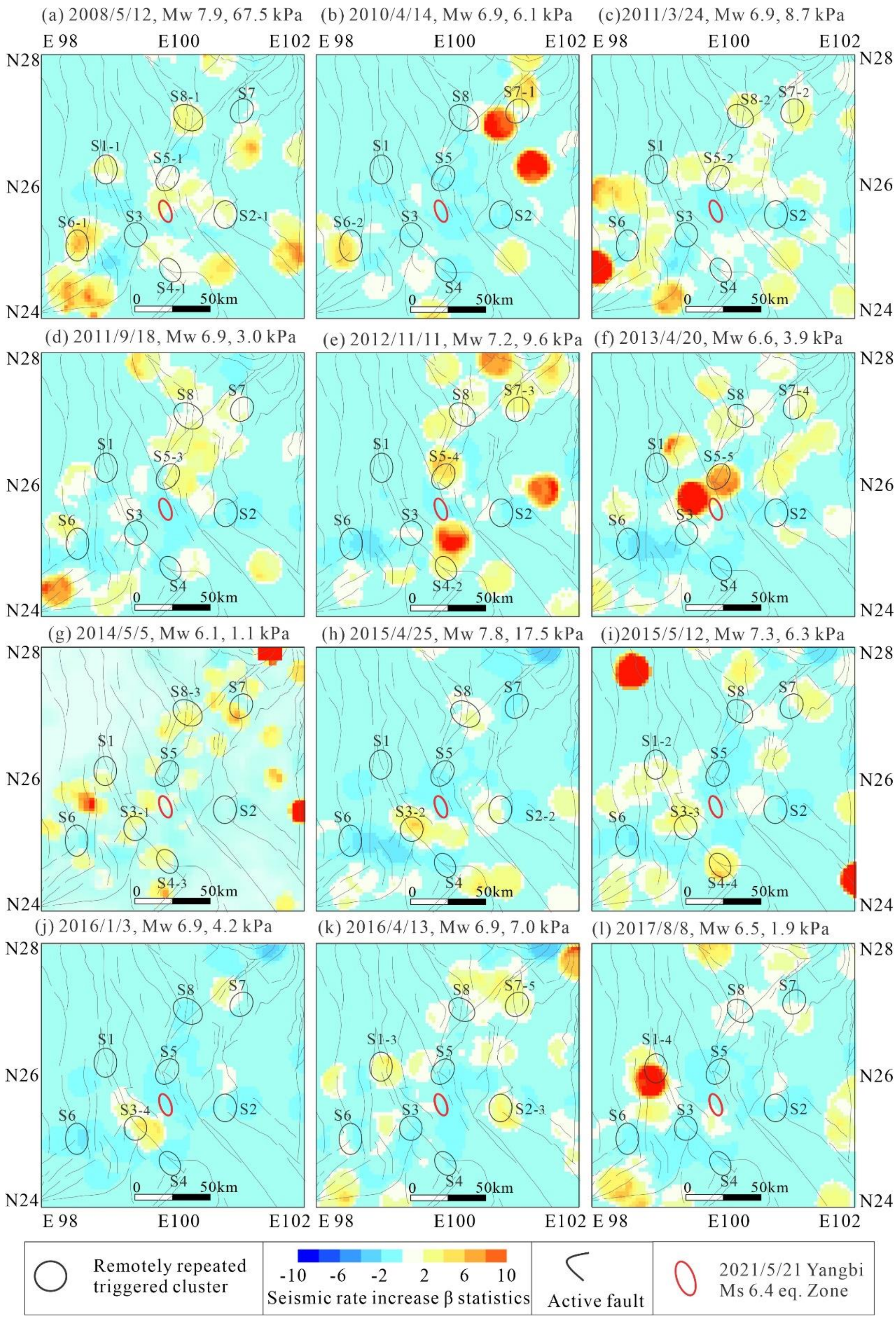

Figure 3. The spatial distribution of β-statistics corresponding to 12 distant M > 6 strong earthquakes is shown in Figure 1. Si-j designates clusters, where 'i' represents the clustered index, and 'j' indicates the number of instances triggered in that cluster

thus far. Stress values labeled on top is the minimum dynamic peak stress value calculated in Table 1.

Table 1. The peak dynamic stress from 13 long-distance strong earthquakes, with the 13th (Laos earthquake) discussed later in the text.

Number	Name	Date Y/M/D	Mw	Epicentral distance range (°)	Peak dynamic stress σ_{pd} range (kPa)
1	Wenchuan	2008/5/12	7.9	(3.28, 8.79)	(67.53, 347.15)
2	Yushu	2010/4/14	6.9	(5.41, 10.69)	(6.13, 15.15)
3	Myanmar	2011/3/24	6.9	(3.67, 7.53)	(8.74, 28.79)
4	Sikkim	2011/9/18	6.9	(9.85, 14.34)	(3.01, 5.60)
5	Myanmar	2012/11/11	7.2	(2.37, 7.95)	(9.60, 47.26)
6	Yaan	2013/4/20	6.6	(2.50, 8.03)	(3.93, 8.00)
7	Thailand	2014/5/5	6.1	(4.65, 8.66)	(1.09, 3.08)
8	Khudi, Nepal	2015/4/25	7.8	(13.27, 17.78)	(17.50, 27.10)
9	Kodari, Nepal	2015/5/12	7.3	(11.94, 16.38)	(6.32, 10.22)
10	Imphal, India	2016/1/3	6.9	(4.42, 8.94)	(4.15, 13.34)
11	Burma	2016/4/13	6.9	(3.26, 8.64)	(6.96, 35.15)
12	Jiuzhaigou	2017/8/8	6.5	(5.51, 10.88)	(1.89, 5.84)
13	Laos	2019/11/20	6.2	(4.59, 9.18)	(1.25, 3.96)

We examined the spatial-temporal migration of seismicity for the ten clusters that experienced repeated triggering to determine whether the seismicity migration front adhered to the hydraulic trigger model $r = \sqrt{4\pi Dt}$ [*Shapiro et al.*, 1997]. In this equation, r represents the distance from the source point of fluid, typically corresponding to the hypocenter of the initial earthquake, to the hypocenter of a given event. The t indicates the elapsed time, and D denotes the hydraulic diffusivity. It is important to note that during the period from 2006 to 2018, the seismic network in Yunnan Province was relative sparse, resulting in limited detection of small earthquakes and lower location accuracy. Consequently, we were able to observe possible fluid-triggering migration fronts in only two clusters, S1 and S5 in Figure 4. These clusters exhibited hydraulic diffusivity values falling within the range from 0.25 to 1.0 m^2/s.

We also observed relatively noteworthy patterns within 14 days in groundwater temperature fluctuations at the LJ-Well, located in close proximity S5, following 12 distant strong earthquakes (Fig. 4). It is important to highlight that in the groundwater circulation system of LJ_Well, deep fluids play a substantial role. The reliability of the groundwater temperature data, which boasts an accuracy of 0.00001°C, has been rigorously verified through on-site instrument testing, observation environment assessment, and adherence to standard calibration procedures [*Y Liu et al.*, 2015].

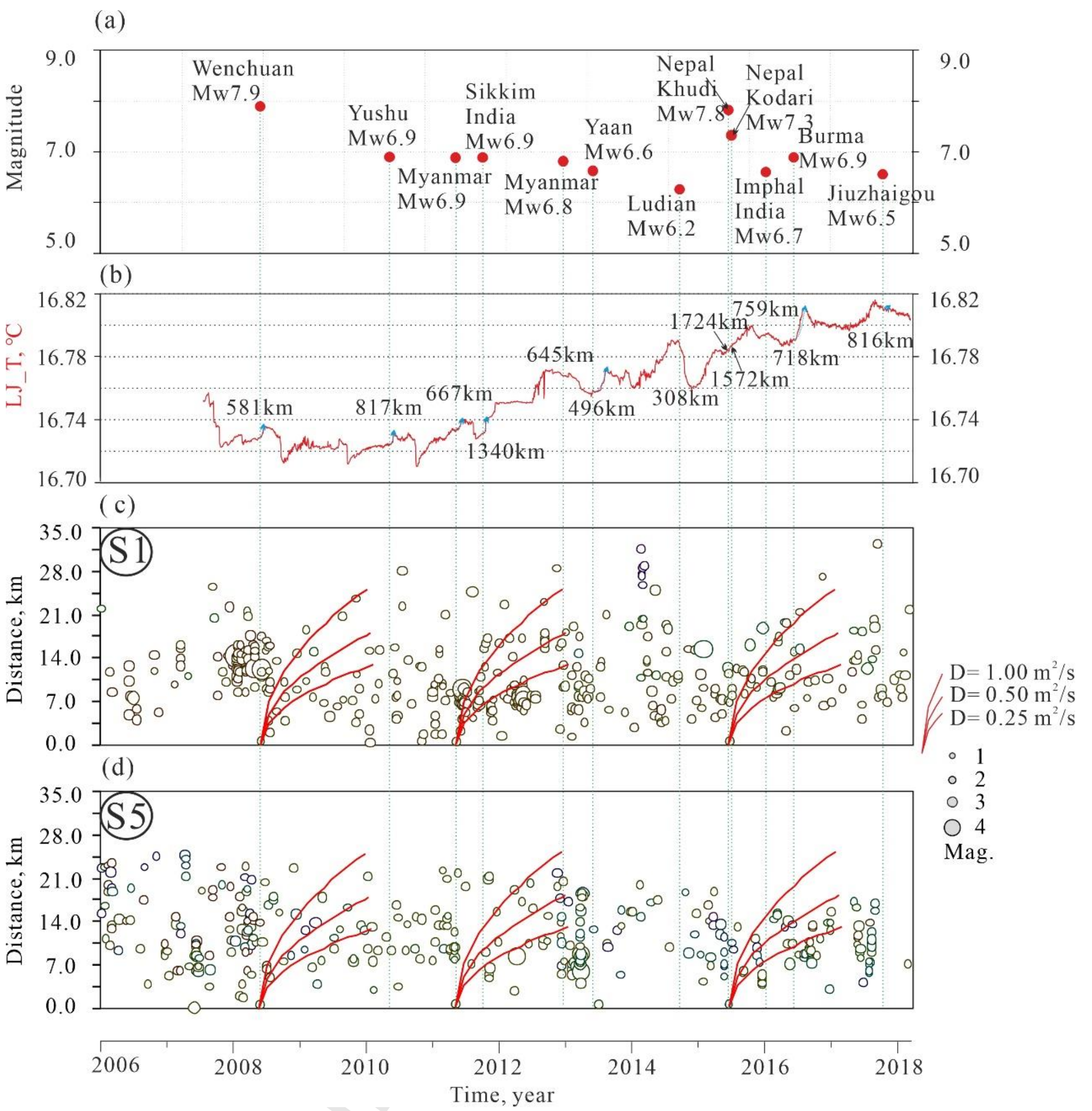

Figure 4. The fluid-triggering migration and water temperature changes with 12 distant strong earthquakes. (a) Magnitude versus time of distant strong earthquakes. (b) LJ_Well water temperature changes with time. The blue dots and blue curves mark temperature changes possibly linked with distant earthquakes. (c) The fluid hydraulic triggering model of the S1 cluster seismicity. (d) The fluid hydraulic triggering model of the S5 cluster seismicity (See S1 and S5 cluster position in Fig. 3).

Table 2. Summary of dynamically triggered clusters within 14 days indicated by $\beta \geq \beta_e$ and $\beta \geq 2.0$. The numbering of events in "Distant EQ" corresponds to the numbering in Table 1 under the column "Number", with the 13th (Laos earthquake) discussed later in the text

#	Distant EQ.	Type	β value	β_e	D (m^2/s)	M_{max}

S1	1, 9, 11, 12	S	2.60, 2.71, 2.92, 3.18	1.81, 1.32, 1.48, 1.68	0.25~1.00	4.1
S2	1, 8, 11	M-A.	4.57, 3.23, 3.83	1.13, 1.90, 1.49	0.50~1.25	3.6
S3	7, 8, 9, 10, 13	M-A.	4.70, 4.80, 4.79, 4.85, 5.08	2.15, 2.21, 2.20, 2.23, 2.35	0.50~1.25	4.0
S4	1, 5, 7, 9	S	5.98, 3.52, 2.96, 4.25	2.83, 2.11, 1.71, 1.73	0.25~0.75	3.4
S5	1, 3, 4, 5, 6, 13	S	2.71, 2.98, 2.23, 2.33, 3.38	1.92, 1.98, 1.96, 1.25, 2.01	0.25~1.00	3.6
S6	1, 2	S	6.28, 6.11	2.98, 2.89	0.25~0.75	3.6
S7	2, 3, 5, 6, 11	S	3.05, 3.18, 4.56, 3.22, 3.22	0.49, 0.55, 0.57, 0.57, 1.89	0.25~1.00	3.4
S8	1, 3, 7, 13	S	2.46, 5.69, 2.64, 2.53	1.26, 1.81, 1.47, 1.39	0.25~0.75	3.7
N1	13	S	84.72	3.26	15~20	4.3

*S: swarm, M-A: Main-aftershock, I: Isolated.

4. Seismicity of the detailed observation period (2018 ~ 2021)

Commencing on February 25, 2018, we install 30 temporary stations to facilitate detailed seismic observation. Using the Template Matching and Location method, as described in the Methods section, we conducted earthquake detection and location from continuous waveforms records. While the magnitude of completeness Mc is deduced to 1.0 (Fig. 5), we applied a higher threshold magnitude of 1.5 to the β statistic. This adjustment helps prevent the overestimation of β values when incorporating the detected events into the catalog. But we may have overlooked some potential distant earthquake triggers. The main contribution of template scanning in this study is to provide a more detailed analysis of detected cases. This allows for a relatively better constraint on fluid-triggering and hydraulic diffusivity, as shown in Figure 7.

Our analysis focuses on the seismicity characteristics in Yunnan both before and after the 2019 Mw6.2 Laos earthquake, which occurred approximately 700 km to the southeast. This event generated peek dynamic stress ranging from 1.25 to 3.96 kPa (Table 1). Notably, it triggered 10 seismic clusters within our study area, as indicated by the β statistic (Fig. 6). Prior to the mainshock, the distribution of seismicity in Yunnan was primarily governed by the fault geometry, with seismic activity, including the dynamically triggered clusters mentioned in the previous section, concentrated at fault ends, bends, step-overs, and intersections. Following the Laos mainshock, earthquakes including those that were triggered, continued to be distributed in these distinct locations.

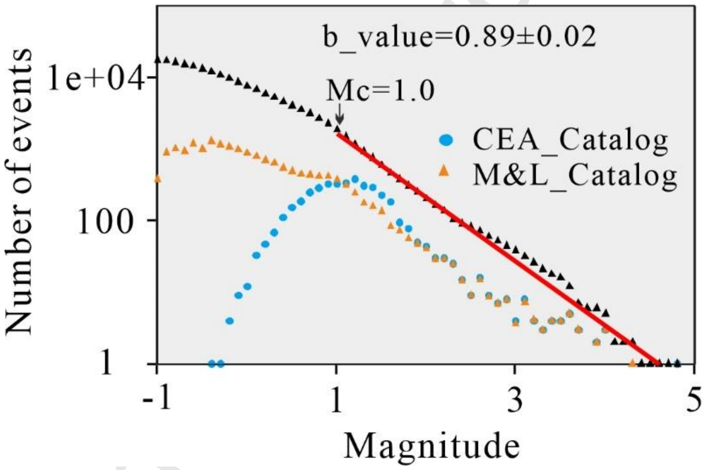

Figure 5. Frequency–magnitude distribution for two seismic catalogues. The blue dots represent the seismic frequency from the catalog provided by the National Earthquake Data Center (CEA). In the template matching method (M&L) catalog: seismic frequency is represented by orange triangles, while cumulative numbers are denoted by black triangles. The seismic b-value, estimated using the Maximum Likelihood Method, is depicted by the red line.

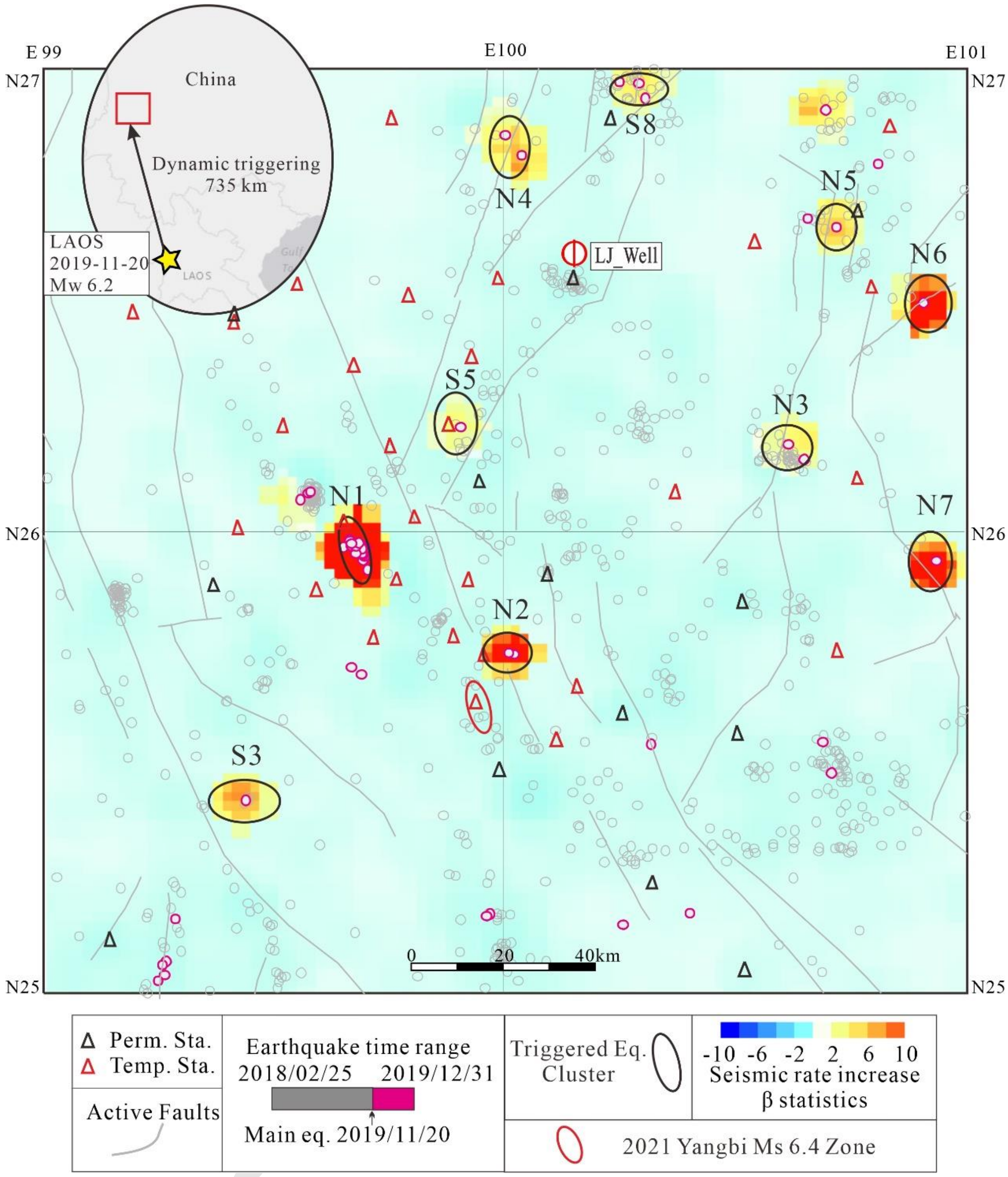

Figure 6. Spatial distribution of seismicity in Yunnan before and after the 2019 Laos Mw 6.2 earthquake. The background color is the β statistics of seismicity increase rate after the Mw 6.2 mainshock. The time window (T_a) of 14 days, the maximum radius distance of 5 km, and the magnitude completeness for the catalog Mc is 1.5. S3, S5, and S8 have the same numbers as the repeatedly triggered clusters in Figure 3. N1 to N7 are newly triggered clusters.

Remarkably, we observed a highly significant dynamically triggered earthquake cluster labeled as 'N1' within close proximity to the seismic stations near Eryuan City

(Fig. 7). In the follows, we will conduct a detailed analysis of this cluster.

The detected and relocated hypocenters vividly depict the seismogenic fault, characterized by a strike of N47.33°W and a dip angle of 72.58°. These parameters were determined through a least squares method fit of the fault plane to the hypocenters.

The onset of triggered seismicity occurred three days after the Laos Mw6.2 earthquake, commencing with events of approximate magnitude 1. Subsequently, about one hour later, a significant M4.3 event occurred. In our analysis, we consider the first M1 event as the injection point. The resulting R-t plot reveals a possible triggering front with D estimated in the range of 15 to 20 m^2/s.

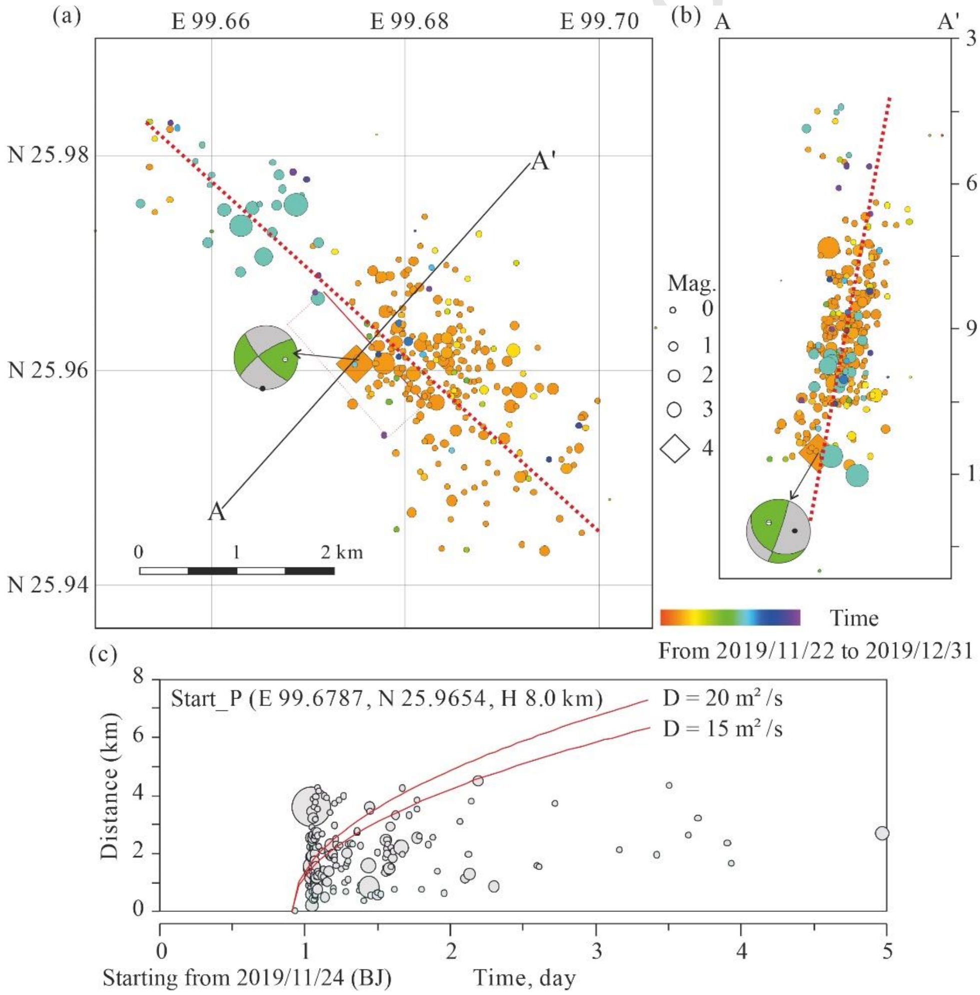

Figure 7. Seismicity migration process at the triggered cluster (N1) after the Mw 6.2 mainshock. (a) Seismicity epicenters distribution of triggered cluster. (b) Seismicity depth profile distribution. (c) Triggering front and estimated hydraulic diffusivity.

Benefitting from the dense seismic network, the magnitude completeness for this cluster is 0.0, as illustrated Figure 8c. The results of the ETAS model with variational forced seismicity indicate that the proportion of forced seismicity accounted for 59.2% (Fig. 8d). Additionally, the magnitude dependence α was 1.114, and the aftershock attenuation coefficient *p* was determined to be 1.43. These parameters show similarities to those observed in the following cases: the fluid signal that initiated a swarm in Bohemia, central Europe [*Hainzl and Ogata*, 2005; *Lei et al.*, 2019; *Lei et al.*, 2011b], injection-induced seismicity in the shale gas field in the Sichuan basin [*Hainzl and Ogata*, 2005; *Lei et al.*, 2019; *Lei et al.*, 2011b], and remotely triggered seismicity in our study region following the 2004 Sumatra earthquake [*Hainzl and Ogata*, 2005; *Lei et al.*, 2019; *Lei et al.*, 2011b]. The resemblance of ETAS results suggests the possibility that the remotely triggered clusters were indeed influenced by deep-seated fluids.

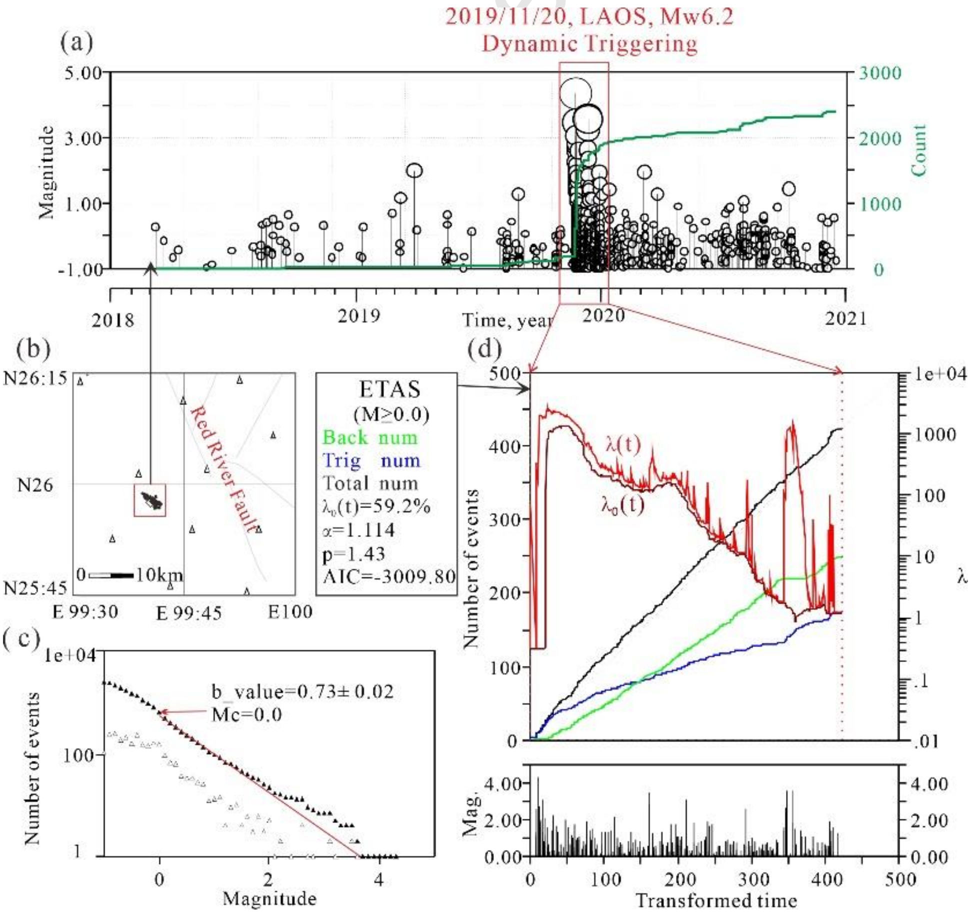

Figure 8. The seismicity at the triggered cluster (N1 in Fig. 6) before and after the Mw 6.2 Laos earthquake. (a) Long-term seismicity varies with time. (b) Map view of

the seismic cluster. (c) Magnitude- frequency distribution for the time span 3 weeks before and 7 weeks after the occurrence of the distant Laos earthquake. (d) Results of ETAS model with time-varying rate of forced (background) seismicity for the same time span of (c). $\lambda(t)$: the total event rate. $\lambda_0(t)$: the background event rate.

Observing Figure 4, we note a consistent upward trend of water temperature at the LJ_Well was observed since 2011. The temperature has increased by approximately 0.14 ℃, with fluctuations of around ±0.02 ℃, shifting from 16.72 ℃ in 2011 to 16.86 ℃ by the end of 2019. For the 2019 Laos earthquake (in Fig. 9), similar to responses observed following other distant earthquakes, the water temperature displayed an immediate increasing trend over 2 days, then returned to a level predicted from the relatively stable trend before the Laos earthquake.

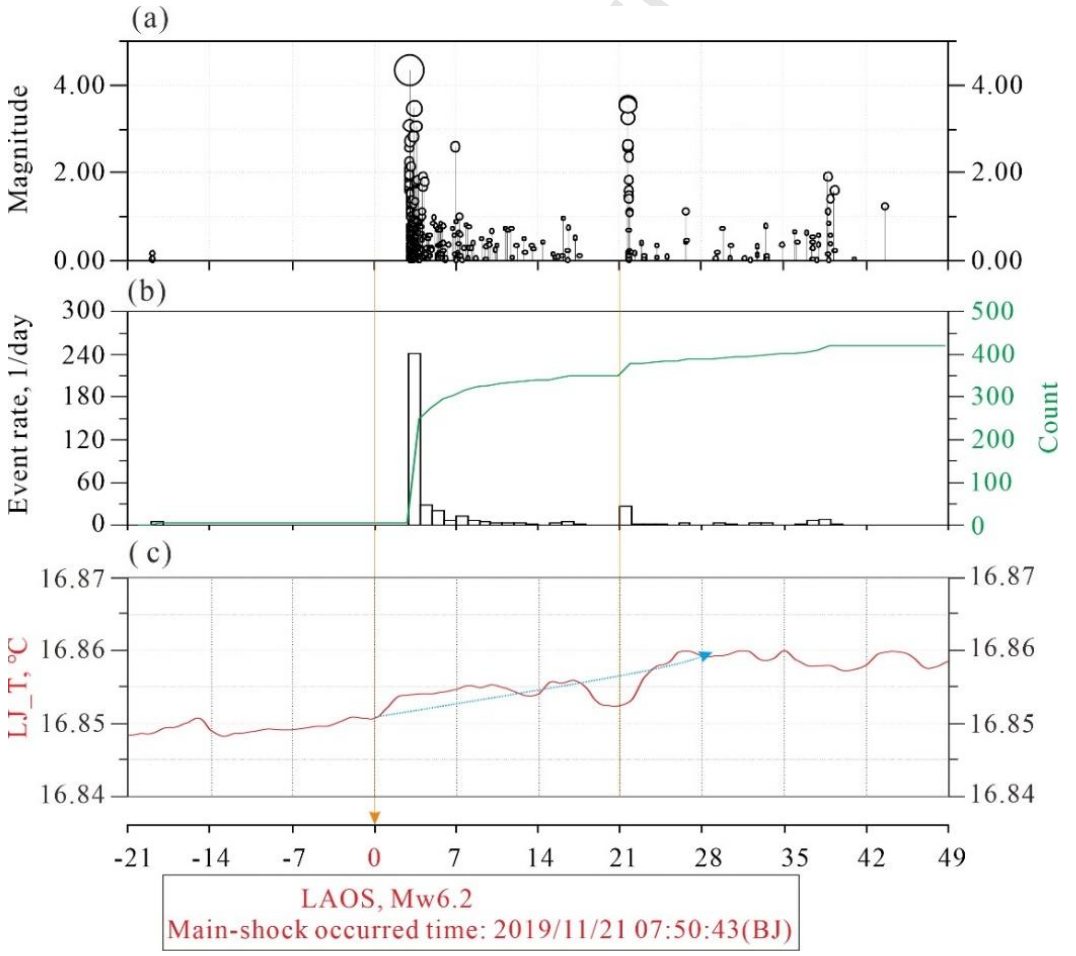

Figure 9. Magnitude (a) and daily event rate (b) for seismicity in cluster N1 (in Fig. 4). Water temperature in LJ well before and after the Mw 6.2 Laos earthquake(c).

5. Discussion and conclusions

In summary, we conducted a systematic analysis of the dynamic triggering impact of global remote earthquakes on seismic activity in geothermally active regions in Yunnan. We found a total of 110 distant earthquakes that triggered peak dynamic stress values exceeding the assumed threshold of 1.0 kPa. Among them, 13 distant events, with a distance less than 20 degrees, triggered seismic clusters at multiple sites. These clusters were predominantly located at specific fault-related spots, including fault ends, fault bends, fault step-overs, and fault intersections. Most teleseismic earthquakes with M> 8.0 did not trigger significant seismicity rate change in our study areas, similar with the Salton Sea Geothermal Field [*C Li et al.*, 2023].

We identified 8 sensitive sites that exhibited repeated dynamic triggering. S2 and S3 clusters, characterized by one or more major events at the beginning, exhibit traits akin to a local main-after sequence or a seismic swarm. Cluster S1, S4, S5, S6, S7 and S8 are categorized as swarm sequences.

The triggered seismicity demonstrating various delay times, similar to what was observed following the 2004 Mw9.3 [*Lei et al.*, 2011a]. Four triggered sequences commenced immediately after the distant event, likely during the passage of surface waves. In contrast, other sequences demonstrated delays up to three days before initiation, such as N1 cluster after the Mw6.2 Laos earthquake.

The triggered sequences of S1, S5 and N1, which boast sufficient number of well-located events, show an efficiently modeled hypocenter migration front through a pore pressure diffusion model. The hydraulic diffusivity ranges from 0.25 to 20 m^2/s. Indeed, the fitting is poor, but falls in the range of hydraulic diffusivity in the upper and middle crust, from less than 0.01 m^2/s to greater than 100 m^2/s, as indicated by some well-constrained cases. For example, in the Tengchong-Baoshan area, which is also within our study area, the hydraulic diffusivity coefficients exhibited by different seismic clusters (well-constrained) spanned four orders of magnitude, ranging from a minimum of 0.02 m^2/s to a maximum of 40 m^2/s [*M Liu et al.*, 2024].

In addition to the triggered seismicity, we noted an upward trend in water temperature in the LJ well. Over the years, the temperature increased by approximately 0.14 ℃, with fluctuations of an amplitude about ±0.02 ℃. Specifically, the temperature rose from 16.72 ℃ in 2011 to 16.86 ℃ by the end of 2019. Importantly, thirteen distant earthquakes that triggered seismicity in the study area were accompanied by an increasing response in water temperature, which was subsequently followed by a transient process lasting over 14 days. This observation suggests that the subsurface temperature field may serve as indicators of dynamic stress variations, providing insight into the interplay between seismic activity and hydrogeological responses.

Based on our comprehensive analysis of the results, we propose that widespread presence of overpressured geothermal fluids in the Yunnan region's crust renders the seismic activity in this area highly sensitive to dynamic stress induced by surface waves from distant earthquakes worldwide. This is a direction worthy of further in-depth research.

Acknowledgment

The present study is supported by the State Key Laboratory of Earthquake Dynamics, the National Key R&D Program of China (No. 2018YFC1503303), and Basic Scientific Funding of Chinese National Nonprofit Institutes (IGCEA2123). Wang Z. acknowledges the support of the State Scholarship Fund of China (No. 201804190004). We use the free software of GeoTaos (https://bemlar.ism.ac.jp/lxl/, developed by Dr. Xinglin Lei at) to do micro-earthquake detection and location, statistical analysis, and draw the figures.

Data Availability

All the data used in this paper are available within the text or accessible through relatively cited references and links.

Reference

Aiken, C., X. Meng, and J. Hardebeck (2018), Testing for the ‘predictability’ of dynamically triggered earthquakes in The Geysers geothermal field, *Earth and Planetary Science Letters*, *486*, 129-140, doi:https://doi.org/10.1016/j.epsl.2018.01.015.

Aiken, C., and Z. Peng (2014), Dynamic triggering of microearthquakes in three geothermal/volcanic regions of California, *J. Geophys. Res. Solid Earth*, *119*, 6992–7009, doi:10.1002/.

Alfaro-Diaz, R., A. A. Velasco, and D. L. Guenaga (2022), Insights from Dynamically Triggered and Induced Earthquakes in Oklahoma, *Seismological Research Letters*, doi:10.1785/0220220211.

Aron, A., and J. L. Hardebeck (2009), Seismicity Rate Changes along the Central California Coast due to Stress Changes from the 2003 M 6.5 San Simeon and 2004 M 6.0 Parkfield Earthquakes, *Bulletin of the Seismological Society of America*, *99*(4), 2280-2292, doi:10.1785/0120080239.

Brodsky, E. E. (2003), A mechanism for sustained groundwater pressure changes induced by distant earthquakes, *Journal of Geophysical Research*, *108*(B8), doi:10.1029/2002jb002321.

Brodsky, E. E. (2006), Long-range triggered earthquakes that continue after the wave train passes, *Geophysical Research Letters*, *33*(15), doi:10.1029/2006gl026605.

Brodsky, E. E., and S. G. Prejean (2005), New constraints on mechanisms of remotely triggered seismicity at Long Valley Caldera, *Journal of Geophysical Research: Solid Earth*, *110*(B4), doi:10.1029/2004jb003211.

Brodsky, E. E., and N. J. van der Elst (2014), The Uses of Dynamic Earthquake Triggering, *Annu. Rev. Earth Planet. Sci.*, *42*, 317–339, doi:10.1146/annurev-earth-060313-054648.

DeSalvio, N. D., and W. Fan (2023), Ubiquitous Earthquake Dynamic Triggering in Southern California, *Journal of Geophysical Research: Solid Earth*, *128*(6), doi:10.1029/2023jb026487.

Fan, F., L. Ye, H. Kanamori, and T. Lay (2021), Responding to Media Inquiries about Earthquake Triggering Interactions, *Seismological Research Letters*, doi:10.1785/0220200452.

Guenaga, D. L., C. Chai, M. Maceira, O. E. Marcillo, and A. A. Velasco (2021), Seismically Detecting Nuclear Reactor Operations Using a Power Spectral Density (PSD) Misfit Detector, *Bulletin of the Seismological Society of America*, *111*(3), 1378-1391, doi:10.1785/0120200267.

Hainzl, S., and Y. Ogata (2005), Detecting fluid signals in seismicity data through statistical earthquake modeling, *J. Geophys. Res.*, *110*(B5S07), doi:10.1029/2004JB003247.

Han, S., H. Zhang, H. Xin, W. Shen, and H. Yao (2021), USTClitho2.0: Updated Unified Seismic Tomography Models for Continental China Lithosphere from Joint Inversion of Body-Wave Arrival Times and Surface-Wave Dispersion Data, *Seismological Research Letters*, doi:10.1785/0220210122.

Hill, D. P., and S. G. Prejean (2015), Dynamic Triggering, in *Treatise on Geophysics*, edited, pp. 273-304, doi:10.1016/b978-0-444-53802-4.00078-6.

Hill, D. P., P. A. Reasenberg, and A. Michael (1993), Seismicity Remotely Triggered by the Magnitude 7.3 Landers.

Johnson, C. W., and R. Bürgmann (2016), Delayed dynamic triggering: Local seismicity leading up to three remoteM ≥ 6 aftershocks of the 11 April 2012 M8.6 Indian Ocean earthquake, *Journal of Geophysical Research: Solid Earth*, *121*(1), 134-151, doi:10.1002/2015jb012243.

Kilb, D., J. Gomberg, and P. Bodin (2000), Triggering of earthquake aftershocks by dynamic stresses, *Nature*, *408*(6812), 570-574, doi:10.1038/35046046.

Lei, X., S. Ma, W. Chen, C. Pang, J. Zeng, and B. Jiang (2013), A detailed view of the injection-induced seismicity in a natural gas reservoir in Zigong, southwestern Sichuan Basin, China, *Journal of Geophysical Research: Solid Earth*, *118*(8), 4296-4311, doi:10.1002/jgrb.50310.

Lei, X., T. Ohuchi, M. Kitamura, X. Li, and Q. Li (2022), An effective method for laboratory acoustic emission detection and location using template matching, *Journal of Rock Mechanics and Geotechnical Engineering*, *14*(5), 1642-1651, doi:10.1016/j.jrmge.2022.03.010.

Lei, X., Z. Wang, and J. Su (2019), The December 2018 ML 5.7 and January 2019 ML 5.3 Earthquakes in South Sichuan Basin Induced by Shale Gas Hydraulic Fracturing, *Seismological Research Letters*, 1099-1110, doi:10.1785/0220190029.

Lei, X., C. Xie, and B. Fu (2011a), Remotely triggered seismicity in Yunnan, southwestern China, following the 2004Mw9.3 Sumatra earthquake, *Journal of Geophysical Research*, *116*(B8), doi:10.1029/2011jb008245.

Lei, X., C. Xie, and B. Fu (2011b), Remotely triggered seismicity in Yunnan, southwestern China, following the 2004Mw9.3 Sumatra earthquake, *J. Geophys. Res.*, *116*(B08303), doi:10.1029/2011jb008245.

Li, C., Z. Peng, D. Yao, X. Meng, and Q. Zhai (2023), Temporal changes of seismicity in Salton Sea Geothermal Field due to distant earthquakes and geothermal productions, *Geophysical*

Journal International, *232*(1), 287-299, doi:10.1093/gji/ggac324.

Li, L., B. Wang, Z. Peng, and D. Li (2019), Dynamic triggering of microseismicity in Southwest China following the 2004 Sumatra and 2012 Indian Ocean earthquakes, *Journal of Asian Earth Sciences*, *176*, 129-140, doi:10.1016/j.jseaes.2019.02.010.

Liu, M., Y. J. Tan, X. Lei, H. Li, Y. Zhang, and W. Wang (2024), Intersection between tectonic faults and magmatic systems promotes swarms with large-magnitude earthquakes around the Tengchong volcanic field, southeastern Tibetan Plateau, *Geology*, doi:10.1130/g51796.1.

Liu, Y., H. Ren, L. Zhang, H. Fu, X. Sun, D. He, H. Yu, Z. Zhou, and G. Zhang (2015), Underground fluid anomalies and the precursor mechanisms of the Ludian Ms 6.5 earthquak, *Seimology and Geology*, *37(1)*, 307-318, doi:10.3969/j.issn.0253-4967.2015.01.024.

Matthews, M. V., and P. A. Reasenberg (1988), Statistical Methods for Investigating Quiescence and Other Temporal Seismicity Patterns, *Pure Appl. Geophys.*, *126*, 357–372, doi:10.1007/BF00879003.

Miyazawa, M., E. E. Brodsky, and H. Guo (2021), Dynamic Earthquake Triggering in Southern California in High Resolution: Intensity, Time Decay, and Regional Variability, *AGU Advances*, *2*(2), doi:10.1029/2020av000309.

Ogata, Y. (1992), Detection of precursory relative quiescence before great earthquakes through a statistical model, *Journal of Geophysical Research*, *97*(B13), 19845, doi:10.1029/92jb00708.

Peña Castro, A. F., S. L. Dougherty, R. M. Harrington, and E. S. Cochran (2018), Delayed dynamic triggering of disposal-induced earthquakes observed by a dense array in northern Oklahoma, *JGR-Solid Earth*, doi:10.1029/2018JB017150.

Peng, G., X. Lei, G. Wang, and F. Jiang (2021), Precursory tidal triggering and b value variation before the 2011 M 5.1 and 5.0 Tengchong, China earthquakes, *Earth and Planetary Science Letters*, *574*, 117167, doi:10.1016/j.epsl.2021.117167.

Peng, Z., and P. Zhao (2009), Migration of early aftershocks following the 2004 Parkfield earthquake, *Nature Geoscience*, *2*(12), 877-881, doi:10.1038/ngeo697.

Perfettini, H., J. Schmittbuhl, and A. Cochard (2003), Shear and normal load perturbations on a two-dimensional continuous fault: 1. Static triggering, *108*(B9), doi:https://doi.org/10.1029/2002JB001804.

Prejean, S. G., and D. P. Hill (2018), The influence of tectonic environment on dynamic earthquake triggering: A review and case study on Alaskan volcanoes, *Tectonophysics*, *745*, 293-304, doi:10.1016/j.tecto.2018.08.007.

Reasenberg, P. A., and R. W. Simpson (1992), Response of Regional Seismicity to the Static Stress Change Produced by the Lorna Prieta Earthquake, *Science*, *255*, 1687–1690, doi:10.1126/science.255.5052.1687.

Shangguan, Z., C. Bai, and M. Sun (2000), Mantle-derived magmatic gas releasing features at the Rehai area, Tengchong county, Yunnan Province, China, *SCIENCE IN CHINA (Series D)*, *43(2)*, 132–140, doi:10.1007/BF02878142.

Shapiro, S. A., E. Huenges, and G. Borm (1997), Estimating the crust permeability from fluid-injection-induced seismic emission at the KTB site, *Geophysical Journal International*, *131*(2), F15-F18, doi:10.1111/j.1365-246X.1997.tb01215.x.

Su, J., X. Lei, J. Li, and C. Huang (2023), Detailed View of the Seismogenic Structures and Processes of the 2022 Bayan Har Intraplate Earthquake Swarm on the East Margin of the

Qinghai–Tibet Plateau, *Seismological Research Letters*, doi:10.1785/0220220336 %J Seismological Research Letters.

Tang, L., Z. Lu, M. Zhang, L. Sun, and L. Wen (2018), Seismicity Induced by Simultaneous Abrupt Changes of Injection Rate and Well Pressure in Hutubi Gas Field, *Journal of Geophysical Research: Solid Earth*, *123*(7), 5929-5944, doi:10.1029/2018jb015863.

van der Elst, N. J., and E. E. Brodsky (2010), Connecting near-field and far-field earthquake triggering to dynamic strain, *Journal of Geophysical Research*, *115*(B7), doi:10.1029/2009jb006681.

van der Elst, N. J., H. M. Savage, K. M. Keranen, and G. A. Abers (2013), Enhanced remote earthquake triggering at fluid-injection sites in the midwestern United States, *Science*, *341*(6142), 164-167, doi:10.1126/science.1238948.

Velasco, A. A., C. J. Ammon, J. Farrell, and K. Pankow (2004), Rupture Directivity of the 3 November 2002 Denali Fault Earthquake Determined from Surface Waves, *Bulletin of the Seismological Society of America*, *94*(6B), S293-S299, doi:10.1785/0120040624 %J Bulletin of the Seismological Society of America.

Voisin, C. (2002), Dynamic triggering of earthquakes: The nonlinear slip-dependent friction case, *Journal of Geophysical Research: Solid Earth*, *107*(B12), ESE 10-11-ESE 10-11, doi:10.1029/2001jb001121.

Voisin, C., F. Cotton, and S. Di Carli (2004), A unified model for dynamic and static stress triggering of aftershocks, antishocks, remote seismicity, creep events, and multisegmented rupture, *Journal of Geophysical Research: Solid Earth*, *109*(B6), doi:10.1029/2003jb002886.

Waldhauser, F., and W. L. Ellsworth (2000), A Double-Difference Earthquake Location

Algorithm: Method and Application to the Northern Hayward Fault, California, *Bulletin of the Seismological Society of America*, *90*(6), 1353–1368, doi:https://doi.org/10.1785/0120000006.

Wang, B., R. M. Harrington, Y. Liu, H. Kao, and H. Yu (2018), Remote Dynamic Triggering of Earthquakes in Three Unconventional Canadian Hydrocarbon Regions Based on a Multiple-Station Matched-Filter Approach, *Bulletin of the Seismological Society of America*, *109*(1), 372-386, doi:10.1785/0120180164 %J Bulletin of the Seismological Society of America.

Wang, Z., X. Lei, S. Ma, X. Wang, and Y. Wan (2020), Induced earthquakes before and after cessation of long-term injections in Rongchang gas field, *Geophysical Research Letters*, doi:10.1029/2020gl089569.

Yao, D., Z. Peng, Y. Kaneko, B. Fry, and X. Meng (2021), Dynamic triggering of earthquakes in the North Island of New Zealand following the 2016 Mw 7.8 Kaikōura earthquake, *Earth and Planetary Science Letters*, *557*, 116723, doi:10.1016/j.epsl.2020.116723.

Yukutake, Y., M. Miyazawa, R. Honda, M. Harada, H. Ito, M. Sakaue, K. Koketsu, and A. Yoshida (2013), Remotely triggered seismic activity in Hakone volcano during and after the passage of surface waves from the 2011 M9.0 Tohoku-Oki earthquake, *Earth and Planetary Science Letters*, *373*, 205-216, doi:10.1016/j.epsl.2013.05.004.

Zhang, M., M. Liu, T. Feng, R. Wang, and W. Zhu (2022), LOC-FLOW: An End-to-End Machine Learning-Based High-Precision Earthquake Location Workflow, *Seismological Research Letters*, doi:10.1785/0220220019.

Zhang, M., and L. Wen (2015), An effective method for small event detection: match and locate (M&L), *Geophysical Journal International*, *200*(3), 1523-1537, doi:10.1093/gji/ggu466.

Zhuang, J., Y. Ogata, and V.-J. David (2002), Stochastic Declustering of Space-Time

Earthquake Occurrences, *Jou. Am. Statist.l Assoc.*, *97*(458), 369–380, doi:https://doi.org/10.1198/016214502760046925

Declaration of interests

☒ The authors declare that they have no known competing financial interests or personal relationships that could have appeared to influence the work reported in this paper.

☐The authors declare the following financial interests/personal relationships which may be considered as potential competing interests:

Highlights:

- Seismicity in the Yunnan area is sensitive to dynamic stress caused by distant strong earthquakes.
- The ETAS models reveal a high proportion of forced seismicity and a weak magnitude-dependent aftershock productivity.
- Triggered clusters repeatedly manifested in specific fault structures with enhanced fluid permeability.